Investigation of ripple phenomenon in hybrid grooved aerostatic bearings

Xiuyuan Chen, Qi Liu, Wenkun Xie, Yi Qin, Xichun Luo*
Centre for Precision Manufacturing, DSMEM, University of Strathclyde, Glasgow, UK
Corresponding. xichun.luo@strath.ac.uk

Abstract
Thrust aerostatic bearings with groove restrictors are major types of supporting components for ultra-precision machine tools and metrology instrument due to their high motional accuracy when moving in a high speed. Ripple is an undesired phenomenon occurred during bearing operation which will reduce the attainable motional accuracy. In this paper, a rapid iterative algorithm based on the resistance network method (RNM) and flow-difference iteration method is proposed to efficiently model and predict the static parameters and the ripple phenomena in the linear grooved (LG) and crossed grooved (CG) thrust aerostatic bearings. The accuracy of the theoretical prediction model is verified qualitatively by computational fluid dynamic (CFD) simulation. It is clearly demonstrated that the ripples of LG and CG thrust aerostatic bearings occur under specific processing parameters at the film thickness of the maximum stiffness. Theoretical modelling and CFD simulating approach for prediction of undesired ripple phenomena is crucial to realize the targets of nanometre or even sub-nanometre positioning accuracy of air bearing supported ultra-precision motional stages.

Keywords Hybrid grooved aerostatic thrust bearing; rapid iterative algorithm; ripple phenomena; computational fluid dynamic simulation

1 Introduction

Aerostatic bearings, feeding a pressurized air into the micrometre level clearance between sliding and static bearing surfaces to support moving parts, have achieved a considerable performance improvement from the aspects of motion accuracy, friction, pollution and speed, compared with precision friction bearings and rolling bearings [1, 2]. During the working state of aerostatic bearings, a specific designed restrictor such as orifice, slot, groove or porous restrictor plays an indispensable role in keeping film pressure balance when the aerostatic bearing affording the external loads [3]. Among various types of restrictors, groove restrictors included LG and CG restrictors can inhibit the pressure decay from orifices to the exit sides of bearing film and provide a more uniform pressure distribution with higher stiffness and load capacity [4, 5]. Though there are several distinctive advantages for these grooved aerostatic thrust bearings, the ripple phenomenon, occurring at the pressure over the center of the ridge is less than the pressure of the sides, can cause bearing instability and this needs to be further investigated. This has some undesirable effect on bearing pressure distribution but of more significance can be the effect on motion error of the moving part in the machine tools [6]. However, an efficient theoretical prediction approach for demonstrating ripple phenomenon is still absent in literature.

Currently, many theoretical predictions are using finite element method or finite difference method based on Reynolds equation to solve the practical engineering problems related to pressure distribution, static stiffness, loading capacity and mass flow rate [7-9]. However, a large number of elements are required to calculate the static and dynamic results of the groove aerostatic bearing directly. Thus, the RNM method makes an assumption that the pressure distribution along the groove width direction can be considered as constant. This assumption was firstly introduced in analyzing the characteristics of T-shape groove aerostatic bearing by Nakamura. et al [10]. Based on this assumption, Chen et al. analyzed the static properties of the thrust aerostatic bearing with X-shaped grooves [11], crossed grooves [12] and arc type grooves [13] by RNM method. It is worthwhile mentioning that the accuracy of RNM method is relatively high. However, inappropriate selection of initial values in these methods can cause lower computation efficiency or even divergence. In this paper, flow-difference iteration method is adopted to reduce the sensitivity to the initial conditions and achieve higher computational efficiency.

CFD simulation has been proved to be an effective way to study the details of flow status inside the aerostatic bearing film, such as the pressure profile, the velocity vector and air vortices [14-16]. Yoshimoto et al. applied CFD simulation to study the pressure distribution of an aerostatic thrust bearing [17]. Eleshaky et al. numerically investigated the pressure depression phenomenon near the orifice through using CFD simulation [18]. Thus, CFD simulation can be used as a reliable tool to predict the pressure profile of the gas film and verify the effectiveness of the established theoretical models.

In this paper, a rapid iterative algorithm is proposed to accurately calculate the static stiffness and loading capacity and efficiently predict the ripple phenomena of the pressure distribution profile in the LG and CG aerostatic bearings. The selection of film thickness associated with the pressure distribution under different structural and processing parameters is determined based on the standard of the maximum static stiffness. CFD simulation is carried out to validate the theoretically predicted ripples occurred under various distance between grooves along the axial direction.

2 Mathematical modeling and solution method

2.1 Theory and governing equation

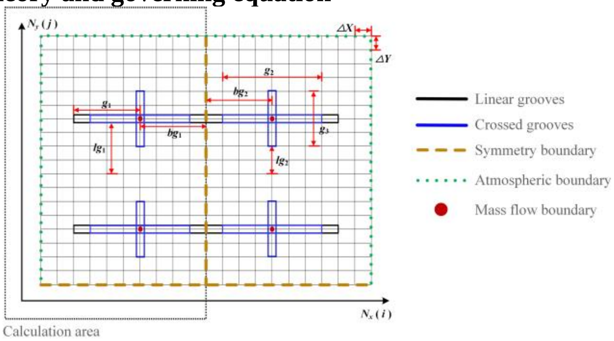

Figure 1: Finite difference mesh and boundary conditions of the air film

The finite difference mesh sketch and the distribution of boundary conditions of the partial LG and CG bearings are shown in the figure. 1. The domain consists of same size grids with number of $N_x \times N_y$ and the calculation area is selected based on the symmetry boundary condition and the LG or CG layouts.

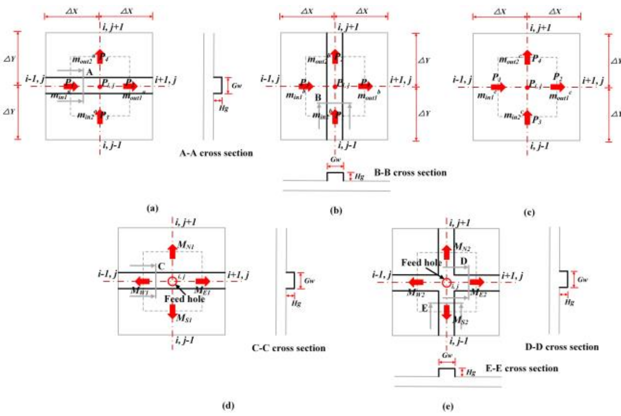

Figure 2: Finite difference grid and control volume by RNM

Figure. 2 shows the partial view of the thrust aerostatic bearing with LG, CG and land area. To calculate the pressure distribution in the reference area of the figure. 2(a), figure. 2(b) and figure. 2(c) (marked as gray dashed square frame), the models based on the principle of continuity of mass flow rate is developed, which can be described as:

$$m_{in1}^{a} + m_{in2}^{a} - m_{out1}^{a} - m_{out2}^{a} = 0 \tag{1}$$

$$m_{in1}^{b} + m_{in2}^{b} - m_{out1}^{b} - m_{out2}^{b} = 0 \tag{2}$$

$$m_{in1}^{c} + m_{in2}^{c} - m_{out1}^{c} - m_{out2}^{c} = 0 \tag{3}$$

Refer to the finite difference equations of the flow in and out of the reference area from published articles [11-13], we can obtain the $P_{i,j}^{2}$ in the horizontal groove, vertical groove and land area of the figure. 2(a), figure. 2(b) and figure. 2(c) through the following equation respectively:

$$(P_{i,j}^{a})^2 = \frac{(P_{i-1,j}^{a})^2 A + (P_{i+1,j}^{a})^2 A + (P_{i,j-1}^{a})^2 B + (P_{i,j+1}^{a})^2 B}{2A + 2B} \tag{4}$$

$$(P_{i,j}^{b})^2 = \frac{(P_{i-1,j}^{b})^2 C + (P_{i+1,j}^{b})^2 C + (P_{i,j-1}^{b})^2 D + (P_{i,j+1}^{b})^2 D}{2C + 2D} \tag{5}$$

$$(P_{i,j}^{c})^2 = \frac{(P_{i-1,j}^{c})^2 E + (P_{i+1,j}^{c})^2 E + (P_{i,j-1}^{c})^2 F + (P_{i,j+1}^{c})^2 F}{2C_1 + 2D_1} \tag{6}$$

$$A = \frac{(\Delta Y - Gw)h_{i,j}^3 + Gw(Hg + h_{i,j})^3}{\Delta X} \tag{7}$$

$$B = \frac{\Delta X h_{i,j}^3}{\Delta Y - Gw/2} \tag{8}$$

$$C = \frac{(\Delta X - Gw)h_{i,j}^3 + Gw(Hg + h_{i,j})^3}{\Delta Y} \tag{9}$$

$$D = \frac{\Delta Y h_{i,j}^3}{\Delta X - Gw/2} \tag{10}$$

$$E = \frac{\Delta X h_{i,j}^3}{\Delta Y} \tag{11}$$

$$F = \frac{\Delta Y h_{i,j}^3}{\Delta X} \tag{12}$$

where *Gw* is groove width, *Hg* is the groove depth and $h_{i,j}$ is the film gap of the bearing at the land region. In these equations, we assume $\Delta X = \Delta Y$.

To solve the continuity equation discussed above, the boundary conditions at the feed hole region which are shown in the figure. 2(d) and figure. 2(e) are expressed as:

$$M_{in1} = M_{N1} + M_{S1} + M_{W1} + M_{E1} \tag{13}$$

$$M_{in2} = M_{N2} + M_{S2} + M_{W2} + M_{E2} \tag{14}$$

where M_{in} is the input mass flow through the feed hole is indicated as follows:

$$M_{in} = aC_D\,\varphi\,\frac{P_s}{\sqrt{R \cdot T}} \tag{15}$$

The value of *a* represents the orifice throat and it depends on the type of feed hole selected. And the φ is the coefficient of orifice outlet flow which also related to the orifice diameter *d*. The calculation equations of the values of *a* and the φ can be referred in reference article [11].

2.2 Process of solving the flux field

The load capacity of the designed thrust grooved aerostatic bearing can be expressed by integration of the pressure distribution over the whole surface area of the air film [17]:

$$W = \int_{-a}^{a}\int_{-b}^{b}(P - P_a)dxdy \tag{16}$$

where P_a is atmosphere pressure and d_x and d_y can be considered as equal to ΔX and ΔY respectively. According to the loading capacity acquired below, the static stiffness *K* of air film can be derived as [17]:

$$K = \Delta W/\Delta h_{ij} \tag{17}$$

In order to improve the efficiency of the searching process, flow-difference feedback iteration method is adopted [18]. The idea of this iteration method is using the relative error E for feedback in the iteration loop of the pressure ratios of orifices β. During the iteration process, the iteration method is variable step-size as the above E changes. Thus, the equation is given as follows

$$\beta^{(k)} = \delta \times \sum_{k=0}^{k_0} \frac{(m_{in}{}^{(k)} - m_{out}{}^{(k)})}{m_{in}{}^{(k)}} \tag{18}$$

where δ is the convergence rate factor, and it usually ranges over [0.01, 0.2]. As explained in the method above, the process to get the solution of flux field is shown in figure. 3.

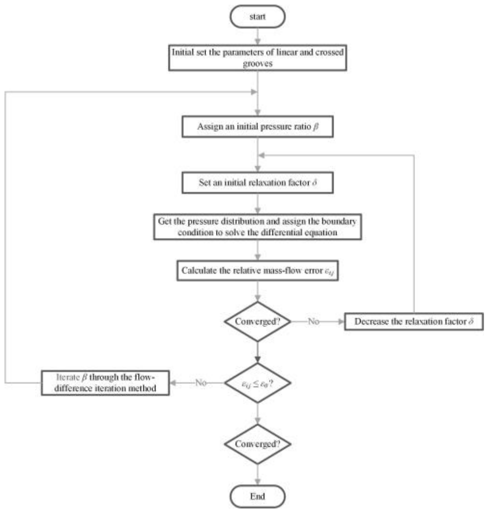

Figure 3: Calculation flow of the aerostatic bearing.

3 Results and discussion

3.1 Load capacity and static stiffness analysis

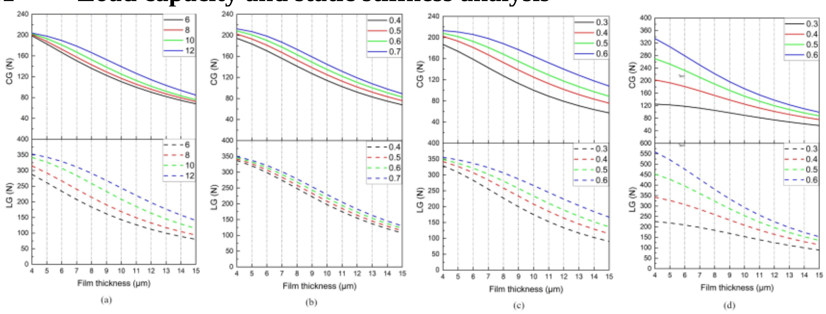

Figure 4: Calculated load capacity under changing (a) groove depth *Hg*; (b) groove width *Gw*; (c) orifice diameter *d*;(d) inlet pressure P_s

As shown in figure. 4, when the groove depth, groove width, orifice diameter and inlet pressure stayed constant, the load capacity decreases as increasing the film thickness. The results from figure. 4 also demonstrated that increasing one of the structural and processing parameters referred above results in greater load capacity when kept other parameters unchanged. But enhancing the groove width has insignificant influence on the load capacity compare to others.

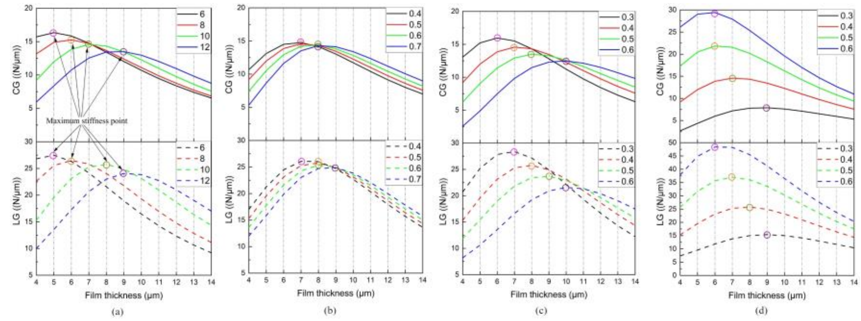

Figure 5: Calculated static stiffness under changing (a) groove depth *Hg*; (b) groove width *Gw*; (c) orifice diameter *d*;(d) inlet pressure P_s

Table1: The film thickness corresponding to the maximum stiffness point

Parameter	value	K (N/μm)	$h_{i,j}$ (μm)	Parameter	Value	K (N/μm)	$h_{i,j}$ (μm)
LG-*Hg*	6 μm	27.47	5	CG-*Hg*	6 μm	16.34	5
LG-*Hg*	8 μm	26.51	6	CG-*Hg*	8 μm	15.26	6
LG-*Hg*	10 μm	25.77	8	CG-*Hg*	10 μm	14.58	7
LG-*Hg*	12 μm	24.05	9	CG-*Hg*	12 μm	13.50	9
LG-*Gw*	0.4 mm	26.07	7	CG-*Gw*	0.4 mm	14.75	7
LG-*Gw*	0.6 mm	25.35	8	CG-*Gw*	0.6 mm	14.40	8
LG-*Gw*	0.7 mm	24.87	9	CG-*Gw*	0.7 mm	14.29	8
LG-*d*	0.3 mm	28.38	7	CG-*d*	0.3 mm	15.96	6
LG-*d*	0.5 mm	23.69	9	CG-*d*	0.5 mm	13.49	8
LG-*d*	0.6 mm	21.57	10	CG-*d*	0.6 mm	12.48	10
LG-P_s	0.3 MPa	15.35	9	CG-P_s	0.3 MPa	7.88	9
LG-P_s	0.5 MPa	37.01	7	CG-P_s	0.5 MPa	21.84	6
LG-P_s	0.6 MPa	48.35	6	CG-P_s	0.6 MPa	29.42	6

Figure. 5 displays the effects of groove depth, groove width, orifice diameter and inlet pressure on static stiffness. It can be seen that the initial stiffness is proportional to the film thickness but lower stiffness is occurred when enhanced the film thickness exceed the maximum point. In other words, the stiffness curves of these structural and processing parameters are like a ‘bell’ shape. Except increasing the groove width causing small increment in stiffness as shown in figure. 5(b), enhancing one of other three parameters can obviously make the larger stiffness, especially for increasing inlet pressure as shown in figure. 5(c), when kept other parameters constant. Table 1 shows the film thickness of the maximum static stiffness under different structural and processing parameters of the LG and CG bearing.

3.2 Force ripple along radial direction

As shown in figure. 6 and figure. 7, when increasing the thickness of air film, the ripples in the LG became apparent along the radial direction while they occurred randomly for the CG at the film thickness of 7 μm and 10 μm. Although ripples along the radial direction have irregular pattern at the inlet pressure of 0.3 MPa for both LG and CG, it is interesting to observe that increasing the inlet pressure can resist the ripples occurring and make pressure distribution more uniform.

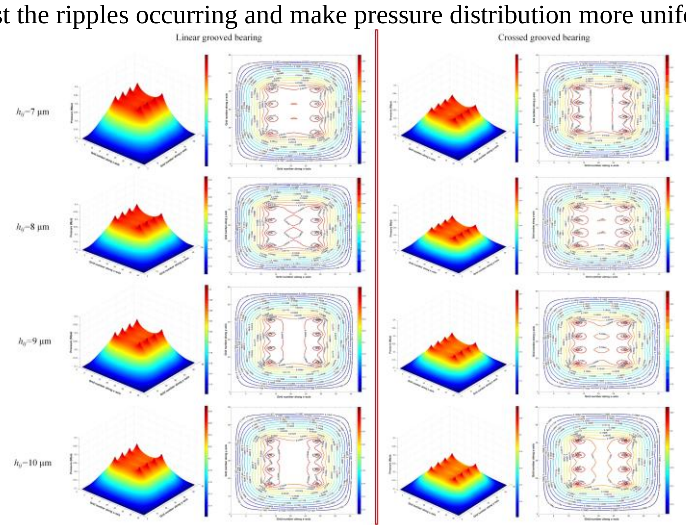

Figure 6: Calculated pressure distribution of LG and CG bearing under changing film thickness (*Gw*=0.5 mm, *Hg*=10 μm, P_s=0.4 MPa, *d*=0.4 mm, g_1=4 mm, g_2=8 mm, g_3=6 mm, bg_1=10 mm, bg_2=10 mm, lg_1=4 mm, lg_2=1 mm)

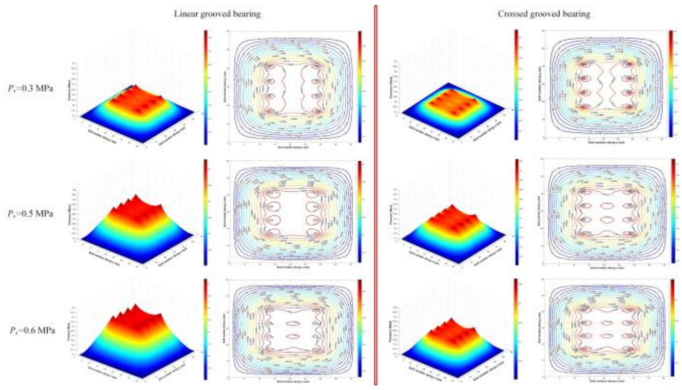

Figure 7: Calculated pressure distribution of LG and CG bearing under changing inlet pressure (*Gw*=0.5 mm, *Hg*=10 μm, *d*=0.4 mm, g_1=4 mm, g_2=8 mm, g_3=6 mm, bg_1=10 mm, bg_2=10 mm, lg_1=4 mm, lg_2=1 mm)

3.3 Force ripple along axial direction

As shown in figure. 8, it was found that the ripples of LG and CG bearing along the axial direction became more significant when increasing the distance between the grooves. And the ripple phenomena became most severe like a series of separated peaks and valleys when the lg_1 and lg_2 increased at 8 mm and 4 mm of the LG and CG bearing, respectively, at the $bg_1 = bg_2 = 5$ mm. Furthermore, these results were qualitatively verified by CFD simulation results of the pressure distribution which as shown in figure. 9(a) and (c). According to the cross section along axial direction of the LG and CG bearing in figure. 9(b) and (d), the curves between the grooves verified calculated ripple phenomena in an intuitive way.

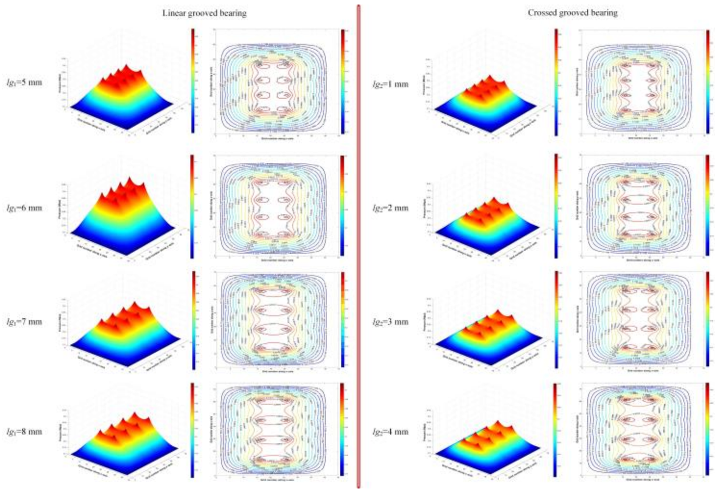

Figure 8: Calculated pressure distribution of LG and CG bearing along axial direction (Gw=0.5 mm, Hg=10 μm, P_s=0.4 MPa, d=0.4 mm, g_1=4 mm, g_2=8 mm, g_3=6 mm, bg_1=5 mm, bg_2=5 mm)

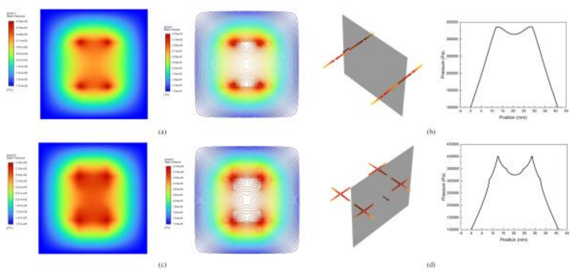

Figure 9: Simulated ripple phenomenon of LG and CG bearing along axial direction

Conclusion

This paper has built a reliable theoretical model to efficiently calculate the static characteristics of thrust grooved aerostatic bearing. The model can be used to optimise its structural and processing parameters more accurately. Besides, investigation of ripple phenomena occurred along radial and axial direction were performed which can help to gain an in-depth understanding of the underlying mechanism of instability of the groove aerostatic bearings under different design and operating situations. In summary, the conclusions can be drawn as follow:

(1) An effective iterative algorithm based on RNM and flow difference iteration method is established to predict accurately the loading capacity, static stiffness and pressure distribution.

(2) Increasing the groove depth, groove width, orifice diameter and inlet pressure can improve the loading capacity of the LG and CG bearings, but it may cause pneumatic hammer when making these referred parameters too large. Besides, the maximum stiffness can be achieved at specific film thickness under different bearing parameters.

(3) The ripples along the axial direction obtained from calculated method have good agreements with the simulated result. This qualitatively verifies the feasibility of applying designed iterative algorithm. As the ripples along the radial and axial directions occurred more randomly at different processing parameters in most cases, it is necessary to use the referred theoretical model and solving method to predict and avoid them to realize the targeted bearing stability and positioning accuracy.

In the future, the prototype of the referred designed hybrid grooved aerostatic thrust bearing will be built to quantify the effect of the ripple phenomenon on the accuracy of machine tools in detail. And a novel interdisciplinary design will also be introduced to restrict or even solve this undesirable ripple phenomenon under different processing and structural parameters.

Acknowledgement

The authors gratefully acknowledge the financial support from the UK Engineering and Physical Sciences Research Council (EP/T024844/1, EP/V055208/1, EP/W004860/1).

References

[1] Altintas Y, Verl A, Brecher C, et al. Machine tool feed drives [J]. CIRP annals, 2011, 60(2): 779-796.

[2] Kawai T, Ebihara K, Takeuchi Y. Improvement of machining accuracy of 5-axis control ultraprecision machining by means of laminarization and mirror surface finishing [J]. CIRP annals, 2005, 54(1): 329-332.

[3] Gao Q, Chen W, Lu L, et al. Aerostatic bearings design and analysis with the application to precision engineering: State-of-the-art and future perspectives [J]. Tribology International, 2019, 135: 1-17.

[4] Nakamura T, et al. Static tilt characteristics of aerostatic rectangular double-pad thrust bearings with compound restrictors [J]. Tribology international, 1996, 29(2): 145-152.
[5] Chen M F, Chen Y P, Lin C D. Research on the arc type aerostatic bearing for a PCB drilling station [J]. Tribology International, 2002, 35(4): 235-243.
[6] Wardle F. Ultra-precision bearings [M]. Elsevier, 2015.
[7] Belforte G, Colombo F, Raparelli T, et al. Performance of externally pressurized grooved thrust bearings [J]. Tribology letters, 2010, 37(3): 553-562.
[8] Chen Y S, Chiu C C, Cheng Y D. Influences of operational conditions and geometric parameters on the stiffness of aerostatic journal bearings [J]. Precision Engineering, 2010, 34(4): 722-734.
[9] Belforte G, Colombo F, Raparelli T, et al. Comparison between grooved and plane aerostatic thrust bearings: static performance [J]. Meccanica, 2011, 46(3): 547-555.
[10] Kogure K, Kaneko R, Ohtani K. A study on characteristics of surface-restriction compensated gas bearing with T-shaped grooves [J]. Bulletin of JSME, 1982, 25(210): 2039-2045.
[11] Chen M F, Lin Y T. Static behavior and dynamic stability analysis of grooved rectangular aerostatic thrust bearings by modified resistance network method [J]. Tribology International, 2002, 35(5): 329-338.
[12] Chen M F, Chen Y P, Lin C D. Research on the arc type aerostatic bearing for a PCB drilling station [J]. Tribology International, 2002, 35(4): 235-243.
[13] Chen M F, Huang W L, Chen Y P. Design of the aerostatic linear guideway with a passive disk-spring compensator for PCB drilling machine [J]. Tribology International, 2010, 43(1-2): 395-403.
[14] Anderson J D, Wendt J. Computational fluid dynamics [M]. New York: McGraw-Hill, 1995.
[15] Cui H L, Wang Y, Wang B R, et al. Numerical simulation and experimental verification of the stiffness and stability of thrust pad aerostatic bearings [J]. Chinese Journal of Mechanical Engineering, 2018, 31(1): 1-12.
[16] Zhu J, Chen H, Chen X. Large eddy simulation of vortex shedding and pressure fluctuation in aerostatic bearings [J]. Journal of Fluids and Structures, 2013, 40: 42-51.
[17] Yoshimoto S, Yamamoto M, Toda K. Numerical calculations of pressure distribution in the bearing clearance of circular aerostatic thrust bearings with a single air supply inlet [J]. Journal of Tribology, 2007, 129(2):384-390.
[18] Eleshaky M E. CFD investigation of pressure depressions in aerostatic circular thrust bearings [J]. Tribology International, 2009, 42(7): 1108-1117.